This is an *Accepted Manuscript*, which has been through the Royal Society of Chemistry peer review process and has been accepted for publication.

Accepted Manuscripts are published online shortly after acceptance, before technical editing, formatting and proof reading. Using this free service, authors can make their results available to the community, in citable form, before we publish the edited article. We will replace this *Accepted Manuscript* with the edited and formatted *Advance Article* as soon as it is available.

You can find more information about *Accepted Manuscripts* in the **Information for Authors**.

Dynamics of high-speed micro-drop impact: numerical simulations and experiments at frame-to-frame times below 100ns

Claas Willem Visser,[1, *] Philipp Erhard Frommhold,[2] Sander
Wildeman,[1] Robert Mettin,[2] Detlef Lohse,[1, *] and Chao Sun[1, *]

[1] *Physics of Fluids Group, Faculty of Science and Technology,*
J. M. Burgers Centre for Fluid Dynamics,
University of Twente, The Netherlands

[2]*Christian Doppler Laboratory for Cavitation and Micro-Erosion,*
Drittes Physikalisches Institut, Georg-August-University Göttingen, Göttingen, Germany

(Dated: December 16, 2014)

1

Abstract

Technologies including (3D-)(bio-)printing, diesel engines, laser-induced forward transfer, and spray cleaning require optimization and therefore understanding of micrometer-sized droplets impacting at velocities beyond 10 m/s. However, as yet, this regime has hardly been addressed. Here we present the first time-resolved experimental investigation of microdroplet impact at velocities up to $V_0 = 50$ m/s, on hydrophilic and -phobic surfaces at frame rates exceeding 10^7 frames per second. A novel method to determine the 3D-droplet profile at sub-micron resolution at the same frame rates is presented, using the fringe pattern observed from a bottom view. A numerical model, which is validated by the side- and bottom-view measurements, is employed to study the viscous boundary layer inside the droplet and the development of the rim.

The spreading dynamics, the maximal spreading diameter, the boundary layer thickness, the rim formation, and the air bubble entrainment are compared to theory and previous experiments. In general, the impact dynamics are equal to millimeter-sized droplet impact for equal Reynolds- Weber- and Stokes numbers (Re, We, and St, respectively). Using our numerical model, effective scaling laws for the progression of the boundary layer thickness and the rim diameter are provided. The dimensionless boundary layer thickness develops in time (t) according to $\delta_{BL} \sim D_0/\sqrt{\text{Re}} \cdot (t/\tau)^{0.45}$, and the diameter of the rim develops as $D_{Rim} \sim D_0/\sqrt{\text{We}} \cdot (t/\tau)^{0.68}$, with drop diameter D_0 and inertial time scale $\tau = D_0/V_0$. These scalings differ from previously assumed, but never validated, values. Finally, no splash is observed, at variance with many predictions but in agreement with models including the influence of the surrounding gas. This confirms that the ambient gas properties are key ingredients for splash threshold predictions.

*c.visser@utwente.nl; d.lohse@utwente.nl; c.sun@utwente.nl (corresponding author).

Keywords: Drop impact — Microdroplet — Superhydrophobic — Printing

I.   INTRODUCTION

Fast impact of small-scale droplets is a key phenomenon in applications such as diesel engines [1, 2], thermal spraying [3], spray cleaning [4], and novel manufacturing technologies based on ink-jet printing technology [5–7] or laser-induced forward transfer [8]. However, the impact of these droplets is often poorly controlled, as it has hardly been visualized. The associated industrial problems include (but are not limited to) defects in metal electronics printing [3, 9], reduced cell survival in spray treatment of burn wounds [10], damage on semiconductor wafers [11], and limited steel strip surface quality [12]. To achieve a better understanding and thereby allow for improved process control, in this article we study the impact of fast, micro-scale droplets on a dry, smooth surface.

This is a challenging task, since for a droplet with diameter $D_0 = 50$ µm impacting at 50 m/s, the impact time scale is $\tau = D_0/V_0 \sim 1$ µs. As this is comparable to the shutter time of high-quality fast cameras, these are still too slow to resolve the details of impact. Much shorter exposure times can be achieved using flash photography [13]. However, with flash photography, only one or two frames per impacting droplet can be captured. Therefore, to obtain multiple frames of the impact using the flash approach, multiple droplet impacts with excellent reproducibility are required. So far, sufficiently reproducible droplets could only be made up to 20 m/s [14–16]. As a result, single-droplet impact at high velocity ($V_0 > 10$ m/s) and small diameters ($D_0 < 100$ µm) has hardly been visualized in detail, despite the vast interest for this subject in the context of the technologies mentioned.

In contrast, major progress has recently been made for mm-sized droplet impact (for background see reviews [34, 35]). We first provide a short overview of the these findings, as they provide the required context for our results on micro-droplets. As schematically shown in figure 1(a), the impacting droplet spreads into a thin lamella until a maximum diameter is reached. The spreading of droplets was shown to be limited by either surface tension or viscosity [21]. The formation of a viscous boundary layer was shown to be crucial [26, 36, 37], and has been included in several experimentally validated models. A self-similar profile of the droplet during spreading was theoretically predicted [36] and recently validated by 3D-measurements of the droplet surface [24]. These articles consistently showed that the
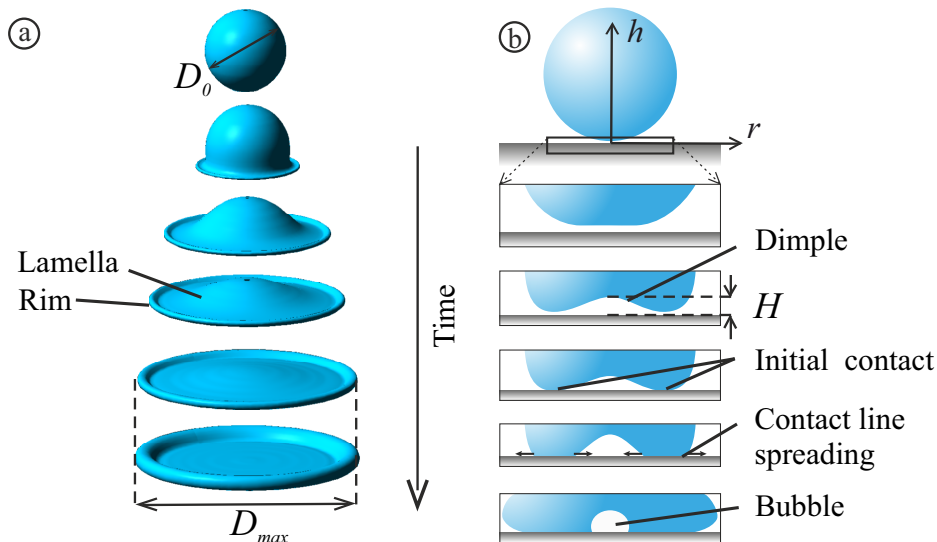
3

FIG. 1: Overview of the different stages of droplet impact. (a) A droplet with diameter D_0 and velocity V_0 is impacting onto a flat smooth surface (only liquid shown). During its spreading into a lamella, a rim is formed. (b) Droplet-substrate interaction in the initial stage of impact, after [17]. The rectangle in the top image is enlarged in the subsequent images, showing snapshots of the cross-section of the droplet. Initially the droplet flattens and forms a dimple, due to compression of the ambient gas between the droplet and the surface. After the initial contact is made, the air under the dimple is entrained and contracts into a bubble.

spreading of an impacting mm-sized droplet can be described sufficiently by the Reynolds number $\mathrm{Re} = \rho D_0 V_0/\mu$ with liquid density ρ, dynamic viscosity μ, and the Weber number $\mathrm{We} = \rho D_0 V_0^2/\sigma$, with surface tension σ. In addition, the droplet-air interaction was found to be crucial in the initial stages of droplet impact [17, 19, 32, 38–41], as schematically shown in figure 1b. Prior to impact, the gap between the droplet and the surface becomes extremely slender, and the escape of the gas from this gap is strongly limited by viscous dissipation in the gas. The trapped gas forms a film between the droplet and the substrate. This film causes a "dimple" in the droplet surface due to the pressure building under the falling droplet, and prevents immediate contact between the droplet and the substrate, see figure 1b. Due to the dimple, the (axisymmetric) minimum of the air film thickness is found off-axis. Eventually, continued thinning of the air film results in contact between the droplet and the substrate, and a wetting front starts running inwards and outwards from the initial, ring-shape contact (indicated by small arrows). The dynamics of the entrapped air can be complex [42–44], but usually the air entrained by the dimple forms a small bubble inside the droplet [14, 44, 45]. The dimple- and bubble-sizes were quantified experimentally,
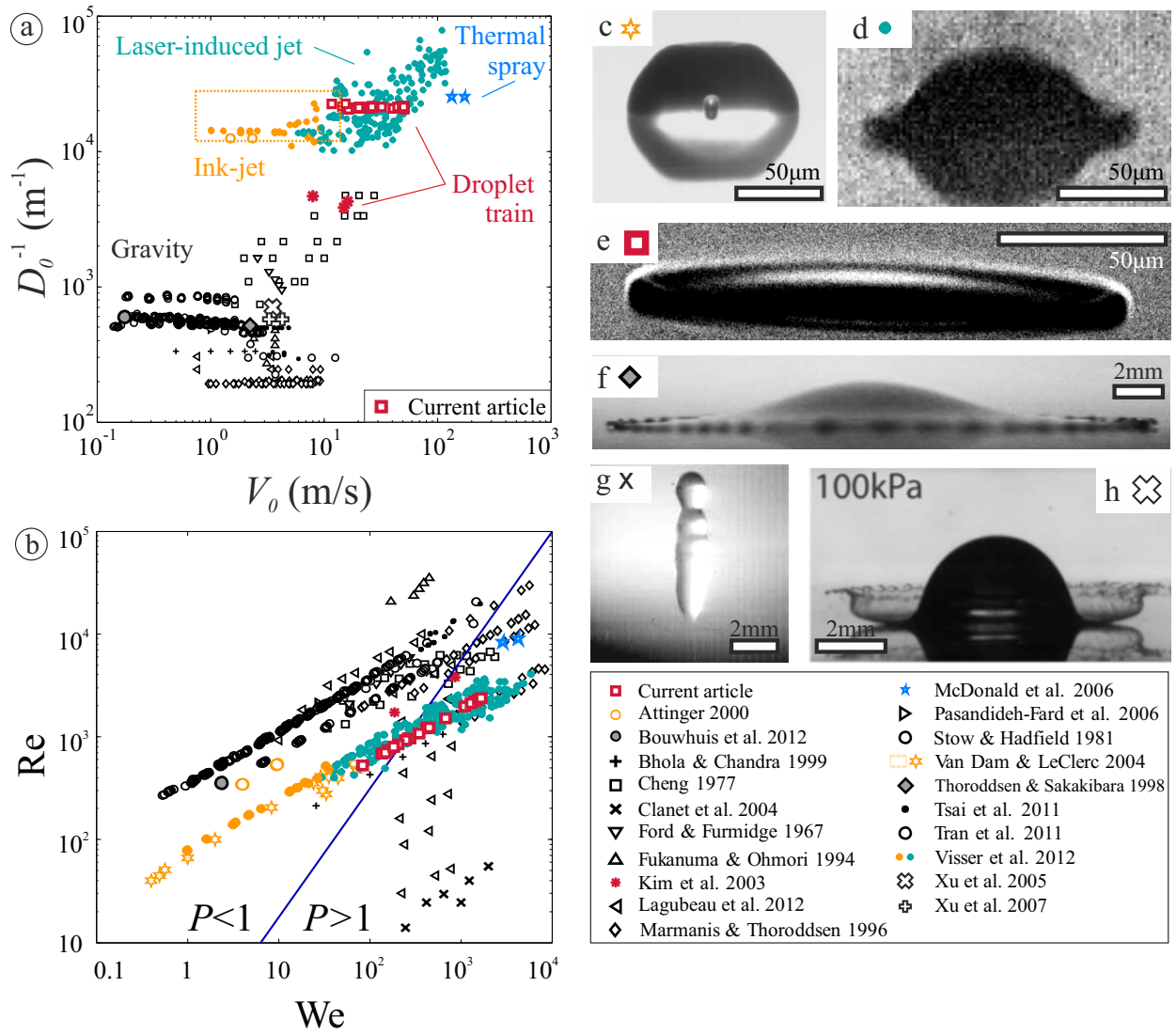
FIG. 2: Overview of experimental work on droplet impact, from refs. [3, 5, 14, 15, 18–33], showing the phase of inverse diameter versus velocity (a) and the Reynolds number versus the Weber number (b). The line indicates the separation between viscosity- and surface tension-dominated regimes (under versus above the line, respectively) of droplet spreading as proposed in ref. [21], and discussed in section III F. Figures (c) to (f) illustrate the wide range of outcomes of droplet impact. Microdroplet impact on a flat surface is shown for water at room temperature in (c), (d), and (e), illustrating the entrainment of an air bubble at low-velocity impact (c) [14], the limited resolution obtained by high-speed camera imaging at high-velocity impact (d) [31], and the development of a rim (e) (current work). Figures (f) to (h) are obtained for mm-sized impact, illustrating rim instabilities (f) [28], bouncing (g) [21], and splashing (h) [32].

numerically and theoretically, using the Reynolds-, Weber-, and Stokes-numbers as control parameters, with Stokes number $St = \rho D_0 V_0 / (2 \mu_g)$, in which μ_g is the gas viscosity [19].

Can these results for mm-sized droplets provide any insight for micro-scale impacts? As

discussed, the parameter space of the impact problem is huge, with the droplet diameter, velocity, viscosity, surface tension, and ambient pressure being the most relevant parameters. A cross-section of this parameters space (the diameter-velocity sub-space) is shown in figure 2a. Even in this limited cross section the phenomenology of the impact problem is extremely rich. Consider for example (c) the entrainment of an air bubble by an impacting microdroplet [14]; (d) a microdroplet during its impact on a flat surface [31]; (e) the development of a thick rim, which for different impact conditions can develop an instability shown in figure 2(f) [33, 46]; (g) a droplet boucing back from a superhydrophobic surface [21, 47, 48]; and (h) splashing of an ethanol droplet on a flat surface [32]. Assuming the relevance of certain forces and processes, one achieves a dimensionless representation of the parameter space as shown in figure 2 (b) (in terms of the Weber- and Reynolds numbers; the Stokes number is the third dimensionless parameter). This shows that the dimensionless control parameters for microdroplet impact coincide to experiments performed for mm-sized droplets (which are performed at a higher viscosity and lower velocity as compared to micrometer-sized droplets, see for example refs. [18, 25]). If the impact problem is scale-invariant, this means that the mm-droplet experiments can be used to obtain accurate predictions for the micro-scale experiments. However, it is not obvious that this scale-invariance must hold. For example the wetting properties of sessile macro-and microdroplets can be rather different [49], due to different contact angles at the macro-and micro-scale. Also, the other dimensionless parameters may become relevant at small scales. Thus, it is a priori unclear whether different dimensional representations of the same point in the dimensionless subspace of the impact problem indeed show the same behavior – this depends on whether the assumptions regarding the relevant processes and forces are correct.

In this work we provide a comprehensive analysis of microdroplet impact employing novel experimental and numerical methods discussed in section II. We visualize for the first time the impact of fast ($V_0 \gg 10$ m/s) microdroplets at high resolutions in section III A, using an interferometric approach to extract the 3D-profile of the droplet surface during spreading at sub-micron resolution. In the subsequent sections we use the numerics and experiments to analyze the spreading dynamics, the air entrainment, the boundary layer flow, the development of a rim, the maximal spreading, and the splashing threshold, and compare these results to those obtained for mm-scale droplets.

II.   DROPLET GENERATION, VISUALIZATION, AND MODELING

A.   Droplet generation

To obtain high-resolution images of fast droplet impact on a glass substrate, we create highly reproducible microdroplets (both temporally and spatially), analogous to what was done in refs. [15, 50, 51]. Figure 3 shows an image of our setup. We first produce a liquid jet by pumping distilled water through a $\sim$20 μm orifice. Using an acoustic element the jet is vibrated at a controlled frequency, forcing Rayleigh break-up of the jet into a train of monodisperse droplets. By applying a positive electrical pulse of duration $\sim \tau$ to the charging electrode, the tip of the jet is temporarily charged negatively at the moment of break-up, and a charged droplet is created. When traveling in the electric field between the deflection plates, this droplet is slightly deflected ($\theta < 1°$). Catching away the droplet train then results in impact of a single droplet on the impact plate, at a velocity controlled by the jet velocity. Three surfaces were used to assess the influence of the macroscopic advancing contact angle θ for droplet spreading: Clean glass, with $\theta = 23°$; RainX, a windshield-repellency coated glass surface (brand: RainX) with $\theta = 90°$, and a hydrophobized aluminium oxide surface [52] with $\theta = 135°$. To prevent charge build-up, the capillary tube, the impact plate, and the reservoir were grounded. The parameter space that was scanned with the current setup is shown in figure 2a (all experiments were performed in air at standard conditions).

B.   Droplet visualization

To visualize the droplet from the side, a double-shutter camera (Sensicam QE, PCO AG, Germany) was used. A 6 ns pulse from dual-flash ND:YAG laser (Quantel, France) provided bright-field illumination. To prevent fringes, coherence was removed by inserting a fluorescent plate in front of the laser. A bottom view was realized similar to the side view. A half-mirror was added to achieve co-axial, dark-field illumination. The camera- and laser timings were synchronized for the side- and bottom-views. All temporal delays were controlled using pulse generators (Berkeley Nucleonics Corporation, model 575).
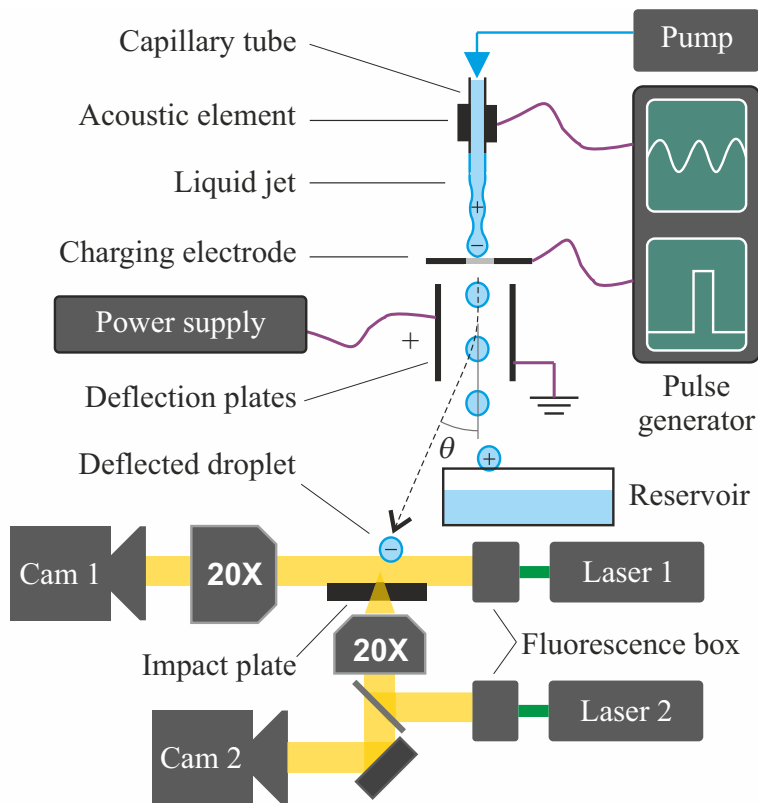
7

FIG. 3: Setup. A liquid jet is created by pumping the liquid through a 20 μm-sized orifice. The jet is acoustically oscillated, to force its break-up into a train of monodisperse droplets. A high-voltage pulse is applied to a charging electrode, just before break-up into a droplet. This charges the jet tip, resulting in a single, charged droplet. This droplet it deflected from the non-charged droplet train by an electrical field. Catching away the droplet train then results in a single, highly reproducible impact on the impact plate. Synchronized side- and bottom views are used for visualization.

C. Determination of droplet size, velocity, and moment of impact

For each experimental setting, the droplet size and velocity were determined as displayed in figure 4. From two side-view images of the in-flight droplet, indicated as 1A and 1B in figure 4a, the droplet position was obtained by automated image analysis in MATLAB (MathWorks Inc., Natick, MA, 2013). As the delay between the frames Δt is known, the spatial difference Δy_1 readily provides the droplet velocity $V = \Delta y_1 / \Delta t$. For each experimental setting, at least 10 image pairs were processed to obtain a velocity histogram as plotted in figure 4b. From this histogram, the median velocity provides the per-experiment velocity V_0. In all cases, the velocity has a typical standard deviation of $0.01 V_0$. The droplet diameter was obtained from frame 1A and 1B of the velocity calibration measurements and each first frame of the impact experiments (frame 2A), resulting in ∼150 diameter measurements for
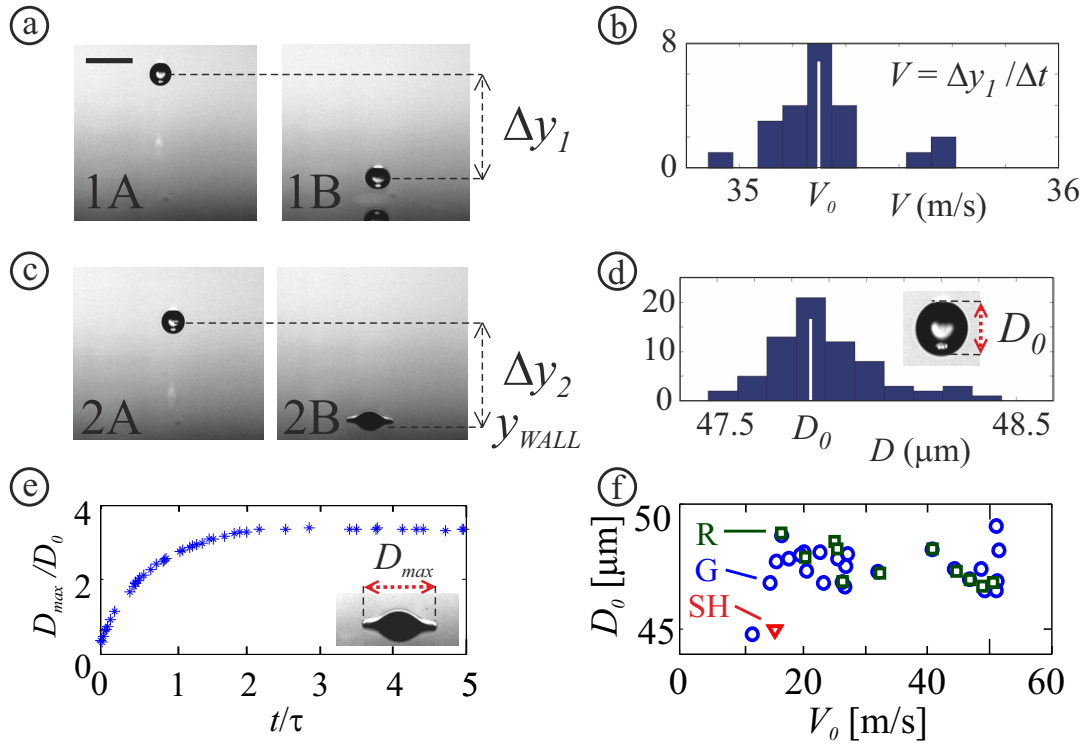
FIG. 4: Determination of droplet size and velocity. All images shown are for equal droplet generation settings. (a) Two in-flight frames are used to determine the droplet translation Δy_1. The translation is used to obtain the droplet velocity. The scale bar indicates 100 μm. (b) Velocity histogram. The median provides the impact velocity V_0. Here and in (d), note the scale of the velocity axis: the distribution is very narrow. (c) Droplet captured in-flight (frame 2A) and during spreading (frame 2B). Frame A is used to collect the diameter D for each experiment. (d) Diameter histogram. The median provides the droplet diameter for each experimental setting, D_0. (e) Example curve of D_{max}/D_0 is plotted versus time. The maximum spreading diameter D_{max} is determined from frame 2B. (f) Parameter space of D_0 and V_0. The markers indicate the surface type (G: Glass ($\theta = 23°$), R: RainX ($\theta = 90°$), SH: Superhydrophobic ($\theta = 135°$)).

each experimental setting. A histogram of the droplet diameter is plotted in figure 4d. Again the median provides D_0 with a typical standard deviation of $0.01D_0$.

An example impact experiment is shown in figure 4c, where frame B shows a clear image of the impacting droplet. However, the arrival time of the droplet has an uncertainty of $\sim$ 1μs due to the 1% uncertainty in the droplet velocity. This is similar to the typical impact time τ, thus a more accurate time determination is required to resolve the impact dynamics. Therefore, for each image pair, we first calculate the time difference between the first droplet-substrate contact and frame A as $t_A = -\tau/2 - \Delta y/V_0$, with Δy the distance between the droplet and the substrate. This yields a negative value, as time $t = 0$s is defined as the moment of impact. The time of frame B is $t_B = t_A + \Delta t$, with Δt the frame-to-frame

delay as set with the pulse generator. The per-frame time uncertainty using this method is 100ns $\ll \tau$, i.e. sufficient for our measurements. To scan the temporal axis of the full impact, this procedure is repeated $\sim$150 times for each experimental setting, with different delays. High-speed movies of the side- and bottom view are constructed for each experiment (example movies are provided for control parameters listed in table S1 and figure S1).

D. Numerical methods

Simulations were done using the open-source flow solver Gerris [53], which numerically solves the incompressible Navier-Stokes equation on a non-uniform flow-adaptive grid. The interface-tracking volume of fluids (VOF) implementation in Gerris makes it well-suited for problems involving two phases with a high density ratio and interfacial tension (water and air). In our axisymmetric simulations we take a uniform grid inside the droplet with typically 340 points across the diameter (i.e. 0.15 μm grid cell size for a $D_0 = 50$ μm droplet). The interface of the drop is adaptively discretized, ensuring that the curvature per cell does not exceed 5% of the droplet radius. The minimum resolution is limited to the resolution inside the droplet. Outside the droplet the grid is adapted according to the norm of the vorticity, with a maximum grid size equal to that of the droplet. The size of the (squared) simulation domain is 3 droplet diameters, with outflow boundary conditions on the top and left edge, no-flow conditions on the bottom edge and symmetry conditions on the right edge (which represent the z-axis along which the droplet approaches the surface). During the downward impact, the air-layer between the droplet and the bottom surface is given extra resolution to prevent the VOF-interface from coalescing with the wall (which also allows for bigger time steps). In most simulations there remains a minimum gap of about 20% of a droplet grid cell (i.e. 30 nm) between the bottom of the domain and the droplet interface. As the viscosity and density do not sharply change over the interface, this means that the droplet is effectively in contact with the no-slip bottom edge at these points (with a 180° contact angle at the contact line).

Example results of the model are shown in figures 1a and 5. The model is validated versus our measurements in figures 6, 8, 9, and 14, as will be discussed in the corresponding subsections of this article.
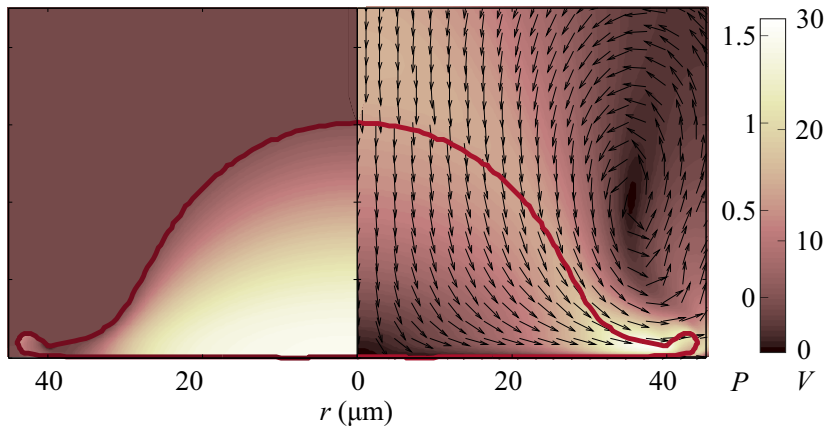
10

FIG. 5: Simulated droplet impact. Left half: Pressure field; the color map indicates the pressure P in 10^5 Pa. Right half: Velocity field, in which the arrows and the colors respectively indicate the flow direction and flow velocity (in m/s). Simulation parameters: $D_0 = 50$ μm and $V_0 = 17$ m/s, corresponding to We = 195 and Re = 836. The snapshot is taken at $t/\tau = 0.42$.
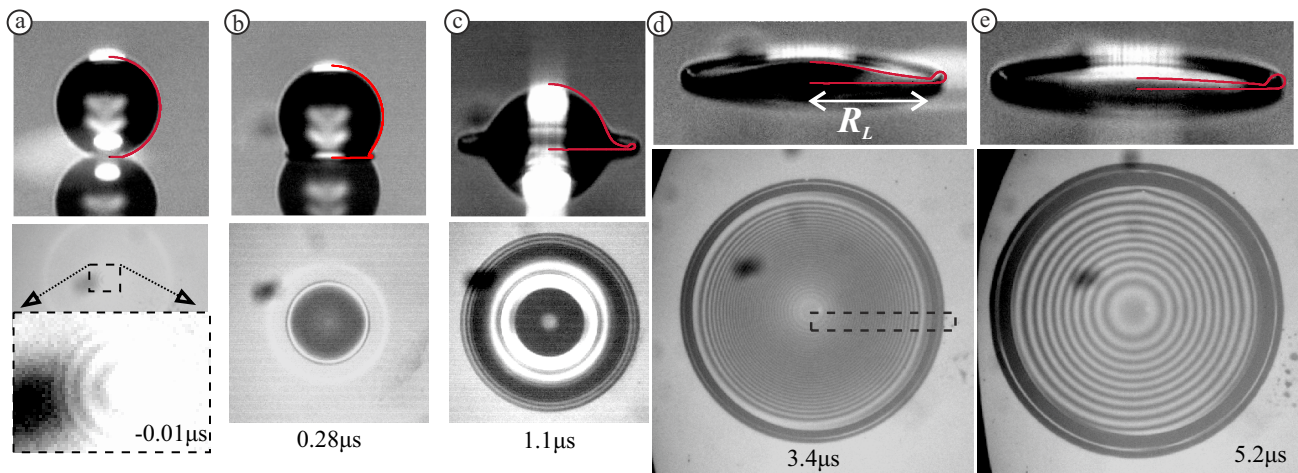

FIG. 6: Side- and bottom-view snapshots of a water droplet impacting onto dry glass for five different times (displayed in the bottom-view images). The side views include the numerically obtained droplet contour (red line, plotted in the right half of the image, see main text). The dark, blurred spots in the bottom view are caused by dirt on the bottom side of the glass. The insert in figure (a) shows air-fringes (explained in main text). The dashed rectangle in figure (d) is magnified in figure 7a. Impact parameters: $D = 49.5$ μm and $V = 16.9$ m/s, corresponding to Re = 836, We = 196, and St = $2.2 \cdot 10^4$.

III. RESULTS AND DISCUSSION

A. Droplet profile

From the side- and bottom view snapshots shown in figure 6, we can identify different stages of the droplet impact. Image 6a shows the droplet just before impact. Subsequently, the droplet spreads over the surface into a lamella. As visible in images 6c to 6e, a rim is formed at the edge of the sheet. After reaching its maximal diameter, the droplet retracts (for hydrophobic surfaces) or the contact line pins and the droplet comes to rest after some capillary oscillations. As we focus on the impact dynamics, these stages are not shown here.

Prior to impact, the bottom view reveals faint fringes (figure 6a). These fringes are due to the air film between the droplet and the substrate, and will be discussed in subsection III C. In the later stages of droplet spreading, the bottom view again reveals clear fringes (figure 6d and e). These fringes are due to interference between the top droplet-air interface and the glass or droplet bottom.

We now analyze the droplet surface profile from the fringes in figure 6d, which have been magnified in figure 7a. After radial averaging, the black and white fringes result in the intensity profile shown in figure 7b. The local minima and maxima of this curve were automatically detected using MATLAB and plotted as open and closed circles, respectively. As the droplet thickness is monotonically decreasing in height within the lamella radius (indicated as R_L in figure 6d), each black-to-white fringe transition is associated to a quarter-wavelength step down in height. The resulting profile is indicated by the dotted curve in figure 7c, where the minimum is set to zero as an initial value. However, the fringes only provide the slope of the droplet surface, thus the actual lamella thickness remains to be determined.

To find the actual lamella thickness we calculate the *volume* contained withing the profile plotted in figure 7c, by fitting a third-order polynomial to it (black line) and integrating the resulting curve assuming axisymmetry. This volume, corresponding to area "A" in figure 7c, is much smaller than the actual droplet volume. This is not surprising, as a part of the droplet volume is contained in the rim, and the lamella must have a non-vanishing thickness everywhere. If we assume that the rim contains all excess volume, the profile drawn in figure 7c is obtained, with a large rim and a vanishing lamella thickness just inside the rim.

12

Alternatively, assuming that all excess volume is present below the profile, we obtain the profile without a rim as plotted in figure 7d. The actual profile, which lies in between these two limiting cases, can be obtained with higher precision from the side view. Using the rim size given by the circle in figure 8a and integrating this to obtain the rim volume, both the rim radius and the film thickness are fixed. In figure 8b, the result is plotted using MATLAB (the lighting was set to make the images (a) and (b) correspond, and a mirror image of the droplet was plotted (in black) below the droplet). Finally, in figure 8c, the derived profile is shown to be in good agreement with the numerical result. Theoretical profiles were derived for inviscid impact [36, 54]. However, since viscosity results in the formation of a boundary layer which affects the film thickness for impact on solid surfaces [54], these predictions deviate from our results (in particular, a much thinner lamella with a far larger radial extension is obtained from theory)and are therefore not included. As the numerical results are based on the Weber, Reynolds, and Stokes-numbers alone, the good overall agreement with the experimental droplet profiles provides first evidence for the scale-invariance of the impact events studied here. In the following sections we will discuss the different aspects of the impact in detail.

B.   Spreading dynamics

In figure 9a, the spreading dimensionless diameter D/D_0 is plotted as a function of dimensionless time t/τ, for different Weber- and Reynolds numbers (indicated by symbol shape) and for impact on surfaces with different wettabilities (indicated by marker color). For $t/\tau \lesssim 3$, we found a negligible influence of the contact angle on the spreading radius, as was also observed for mm-sized droplets [55]. Good agreement between our measurements and our numerical model (solid lines) is reached . In fact, even better agreement with the numerical results is obtained than with mm-sized droplets, as in measurements with mm-sized droplets (ref. [55], plotted as *) slightly stronger spreading than in our numerical simulations is seen, for unknown reasons.

To compare our results with the literature, we require a more detailed picture of the spreading dynamics of the droplet. The impact can be divided into three different phases, of which the first two are depicted by the inset in figure 9b:

- The initial phase, in which the bulk of the droplet maintains its initial velocity and no
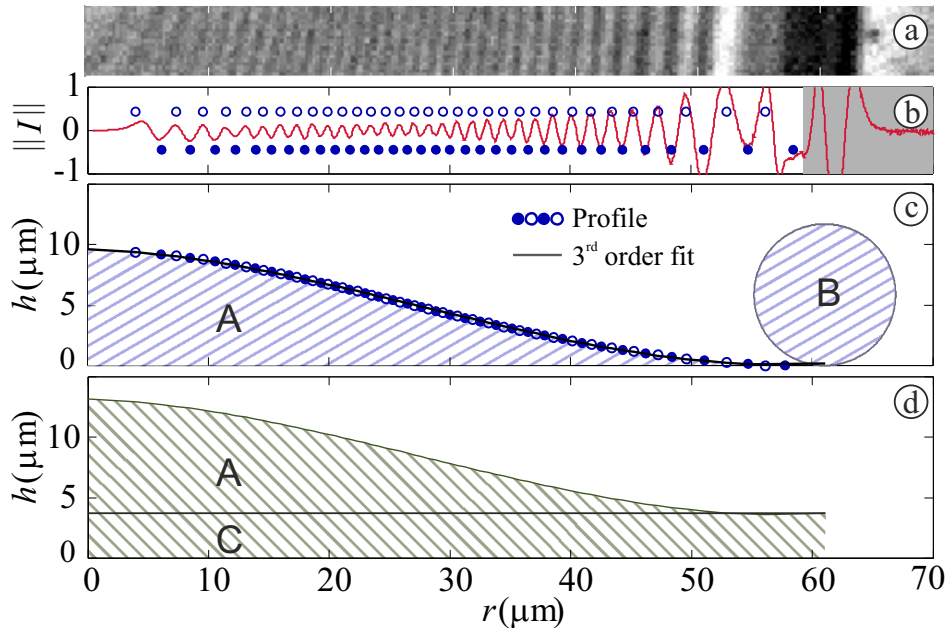
FIG. 7: Bottom view analysis. (a) Detail of figure 6d, clearly showing fringes. (b) Radially-averaged intensity map of the bottom view image. The open and closed markers show the radial positions where respective bright and dark fringes were detected. The shaded area is not used for analysis: (c) The rim profile determined from the fringes is shown by the open and closed markers, corresponding to figure (b). The black line indicates a third-order fit. Integration of area A provides the volume contained under the profile, which is less than the original drop volume. Area B corresponds to the rim volume if the rim would contain all excess volume of the droplet. (d) Area C corresponds to the excess liquid if it would be fully contained under the droplet, resulting in an offset of the droplet profile equal to the height of area C.

lamella is ejected (blue line in the inset of figure 9b). The droplet-substrate contact diameter D_C was initially described assuming compression of the liquid in the droplet (i.e. lack of lamella ejection), resulting in $D_C/D_0 = 2\sqrt{t/\tau - (t/\tau)^2}$ from geometry arguments [55]. A modification was made by assuming incompressible flow from the droplet into a disk-shaped lamella [14, 58], but for $t/\tau \ll 1$ this result collapses to the aforementioned result from ref. [55]. Recently, the radial position of the inflection point D_I was calculated using Wagner's theory [59], resulting in $D_I = \sqrt{3t/\tau}$, and proposed as the initial wetting velocity [56]. As the transition to the next regime (where the lamella is ejected) occurs on a time scale of order $\tau/100$, we could not yet study this regime. To conclusively measure the dynamics in this regime (also for mm-sized droplets), high-resolution measurements would be required, in particular in view of the small differences between the various predictions.
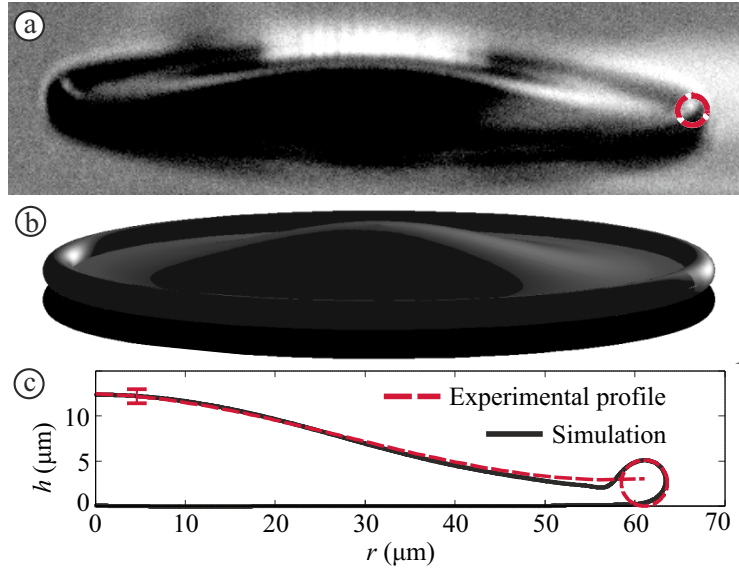
FIG. 8: Bottom view analysis combined with side view and simulation, for the droplet analyzed in figure 7. (a) Side view image. In red the rim size is shown, which was used for the analysis of the bottom view images as explained in the main text. (b) Side-view image reconstructed from the fringes in the bottom-view. (c) Rim profiles determined from experiment and simulation. The red vertical line indicates the experimental error.

- The lamella phase. A lamella is ejected when its velocity exceeds the wetting velocity observed in the initial phase [56, 57]. This occurs at the lamella ejection time t_e, which was recently modeled [56] by the solution of the implicit equation

$$\sqrt{3}/2\mathrm{Re}^{-1}(t_e/\tau)^{-1/2} + \mathrm{We}^{-1} = C(t_e/\tau)^{3/2}, \tag{1}$$

with prefactor $C = 1.2$. For our control parameters this yields a value of $0.02 < t_e/\tau < 0.04$, illustrated by the transition from the shaded (blue) region to the white region in figure 9b. The lamella spreading velocity and radial extension were obtained by equating the inflow from the drop and the outflow into the lamella (modeled as a circular disc with an empirically obtained thickness) [57]:

$$\frac{D_L(t)}{D_0} = 2.9\sqrt{\frac{t}{\tau}}. \tag{2}$$

A comparison with our experimental results in this regime is provided in figure 9c, where the axes were chosen to allow direct comparison to ref. [57]. The experimental results are limited to $4t_e < t < \tau$, ensuring that only the lamella regime is captured.
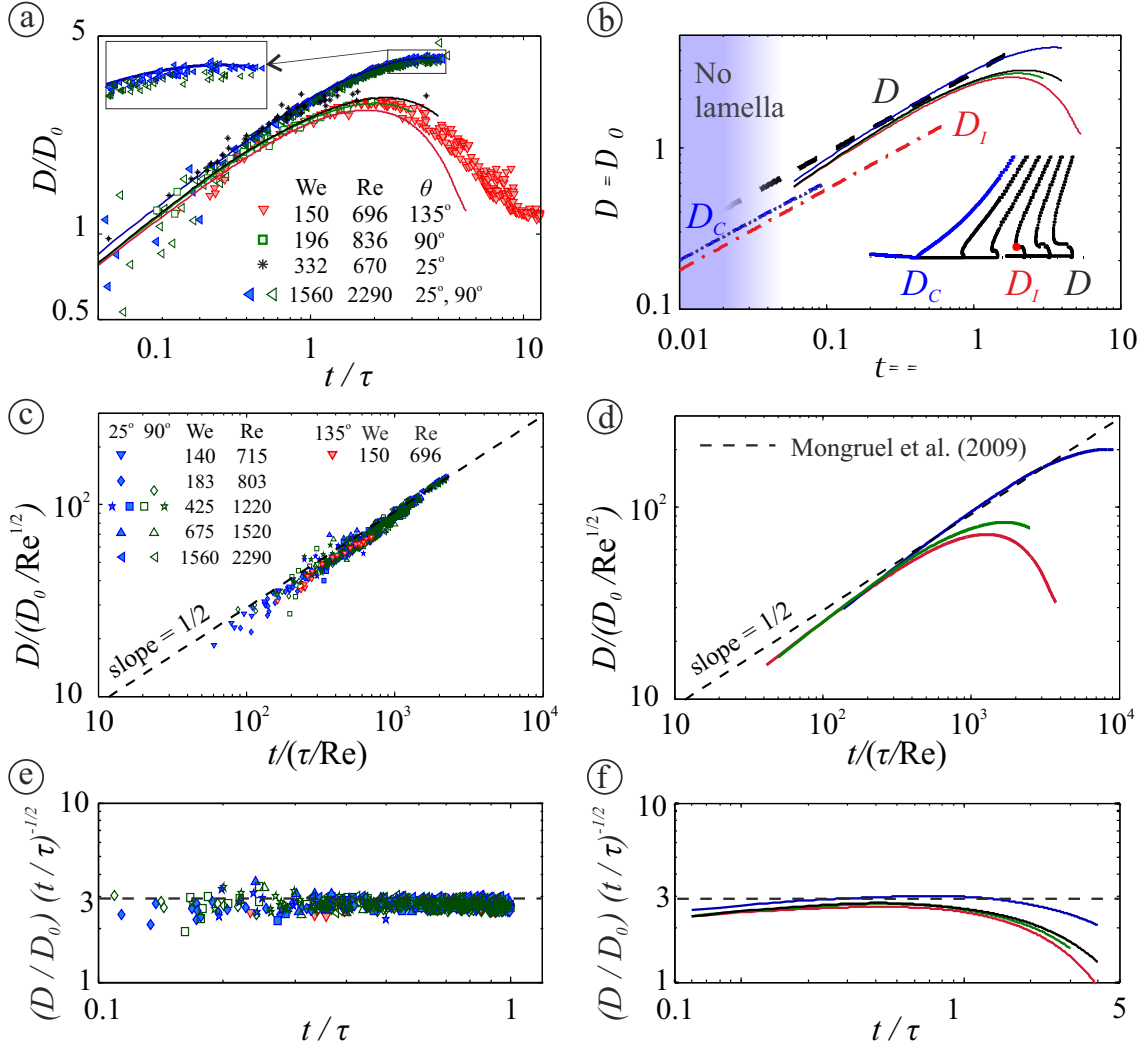
15

FIG. 9: Normalized spreading diameter versus time. Left: (mainly) experiments. Right: numerical results. (a) Comparison between measurements (markers) and simulations (lines) for three different contact angles. The black stars represent mm-sized droplet data from ref. [55] ($D_0 = 2.7$ mm and $V_0 = 2.6$ m/s, We and Re in the legend). The spreading is contact-angle independent and good agreement with the numerical results is obtained, as illustrated by the collapsing curves in the inset. Final retraction of the droplet is observed only for the strongly hydrophobic surface ($\theta = 135°$) and in the simulations ($\theta = 180°$). (b) Development of the contact diameter before lamella ejection D_C (blue dash-dotted line), the inflection diameter D_I (red dashed line), and the maximal lamella diameter D (black dashed line); solid lines show the numerical results corresponding to figure (a). The color-gradient indicates the predicted transition towards the lamella regime [56], as discussed in the main text. A time series of the droplet shape is shown in the right-bottom corner of the figure, illustrating the contact diameter D_C, the inflection diameter D_I, and the maximal lamella diameter D. (c) Normalized lamella spreading versus normalized time. The experimental data (shown for $t/\tau < 1$) collapse to the model proposed by Mongruel et al. [57] (equation (2), shown as a dashed line in figures (c) to (f)) within the experimental error. (d) The numerical results (solid lines) collapse to theory [57] at intermediate times. For small times the lamella is not fully developed; in the late regime surface tension and viscosity limit the spreading. (e) & (f): The corresponding compensated plots $(D/D_0)(t/\tau)^{-1/2}$ versus t/τ (out of which Re cancels) for figures (c) & (d).

16

The model and experiments agree quantitatively within the experimental error, again evidencing scale-invariance of the drop impact dynamics. Our numerical results (figure 9d) show reasonable agreement for intermediate times, but deviate for small times (where the transition from the slower initial regime results in a lower value), and for large times (due to slow-down, next item).

- The slow-down phase ($t/\tau > 1$), in which surface tension and viscosity significantly slow down the spreading lamella. This eventually stops the spreading, defining the maximum spreading diameter as discussed in subsection III F.

C. Droplet-air interaction

As discussed in the introduction and shown in figure 1b, the gas in the gap between the droplet and the surface forms a dimple in the droplet and "cushions" the impact. The initial contact between the droplet and the substrate therefore occurs off-axis, and air is entrained by the dimple in the droplet. As this air cannot escape, a small bubble inside the droplet is observed.

Initially we aimed to assess the air film behavior using the fringes using bottom-view interferometry, a method commonly applied to determine the air profile separating the droplet from the surface [17, 39, 61]. However, processing the fringes shown in figure 6a reveals a spherical droplet profile with a curvature corresponding to the droplet size, i.e. the expected dimple was not observed. A prediction of the dimple height was provided in ref. [19], yielding $H \sim 50$nm for our control parameters. As the resolution of the interference method is limited to $\lambda/4 = 145$ nm (with $\lambda = 577$nm the illumination wavelength) the dimple profile cannot be resolved with bottom-view interferometry in the visible spectrum. Therefore, to assess the scale-invariance of the droplet-air interaction, we now discuss the bubble size.

The size of the bubble entrained by impacting droplets was determined theoretically, experimentally, and numerically for *millimeter*-sized droplets [19], as shown in figure 10. At very low Stokes numbers (i.e. slow droplets), the droplet approaches the surface so slowly that the gas can escape, and no bubble is entrained [62]. For increasing (but still low) Stokes numbers, an increasingly large bubble is observed, indicated by the solid black line in figure 10. However, in the high-Stokes number limit, the gas is squeezed out so strongly
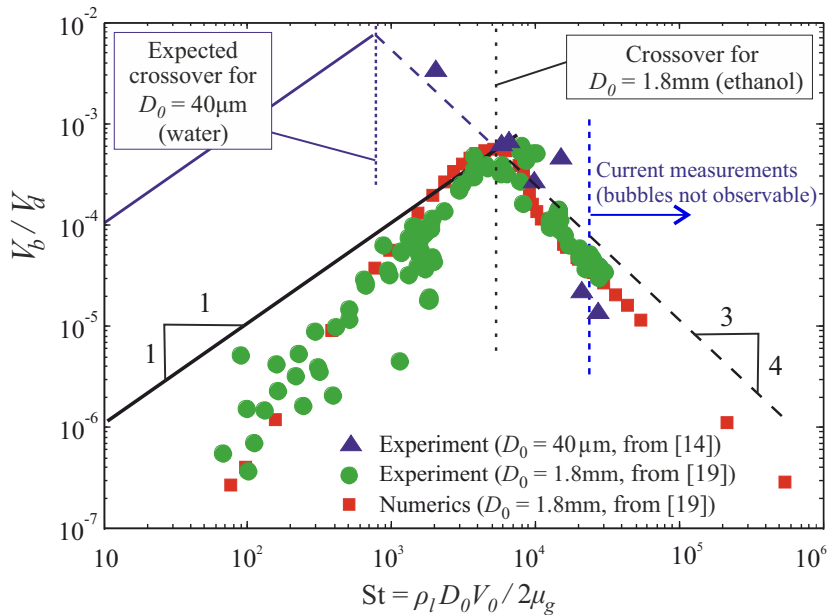
FIG. 10: Dimensionless volume of the bubble entrained during droplet impact versus the Stokes number (St). For microdroplets, the bubble volume was measured by Van Dam and Le Clerc (2004) [14] and re-cast here (blue markers), as for the current experiments the bubble size is smaller than the optical resolution of the setup. For comparison to air entrainment by mm-sized droplets, the experimental and numerical results from Bouwhuis *et al.* (2012) [19] are included (green and red markers). The lines show scaling laws proposed for the capillary air entrainment regime (low-St, solid lines, from ref. [19]) and the inertial air entrainment regime (high-St, dashed lines, from refs. [19, 60]). The vertical blue and black dashed lines indicate the crossover from the capillary to the inertial regime, for micro- and mm-sized droplet impact, respectively.

that again very small bubbles are observed as indicated by the black dashed line [60]. The maximum bubble size is observed at an intermediate "crossover" Stokes number, which is plotted as a vertical dotted line in figure 10.

Since compressibility is likely to become important for fast *micrometer*-sized droplet impact [60, 63], the question is whether equal dimensionless droplet sizes are observed. The bubbles entrained by microdroplet impact at lower velocities than in our experiments[1] were measured by Van Dam and LeClerc [14] and are re-cast in figure 10. To compare these data to the model discussed, the crossover Stokes number (which depends on the Weber- and Reynolds numbers and will thus change for smaller droplets) was re-calculated for $D_0 = 40$ µm and plotted as a blue dotted line in figure 10. The data from ref. [14]

---

[1] Our current experiments (at high Stokes numbers, see figure 10) resulted in a bubble size below the resolution of our setup.
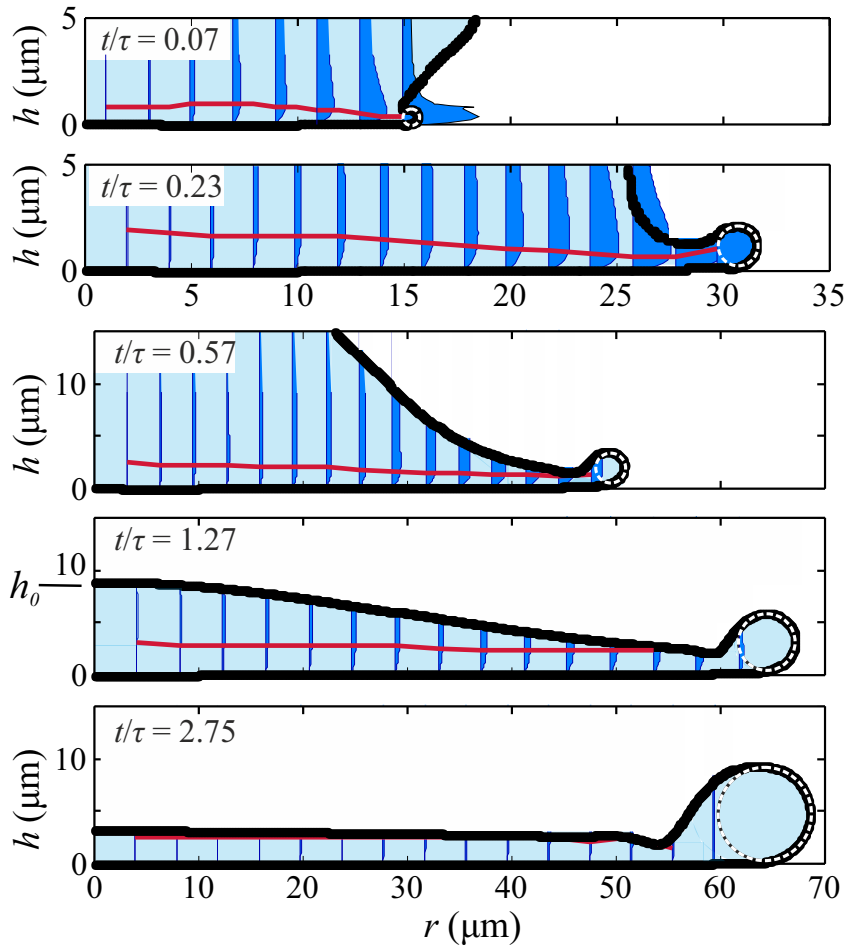
18

FIG. 11: Snapshots of the simulated cross section of the droplet, for We = 196 and Re = 836. The black line indicates the droplet contour, the blue shading indicates the liquid, and the radial velocity component are plotted as filled areas (blue). The red line indicates the boundary layer $\delta(r,t)$. The white dotted lines shows the fitted rim profile. The parameter h_0 indicates the center height of the droplet, as shown left of the fourth image. Note the different scaling of the upper two images, allowing for a more detailed view.

collapse to the prediction, and completely lie in the high-Stokes regime. Although the scale-invariance of the low-St regime remains to be addressed, this provides strong evidence for scale-invariant entrainment of air by droplet impact in the high-St regime, i.e. that no additional dimensionless numbers (apart from Re, We, and St) are required to describe the air entrainment by impacting droplets.
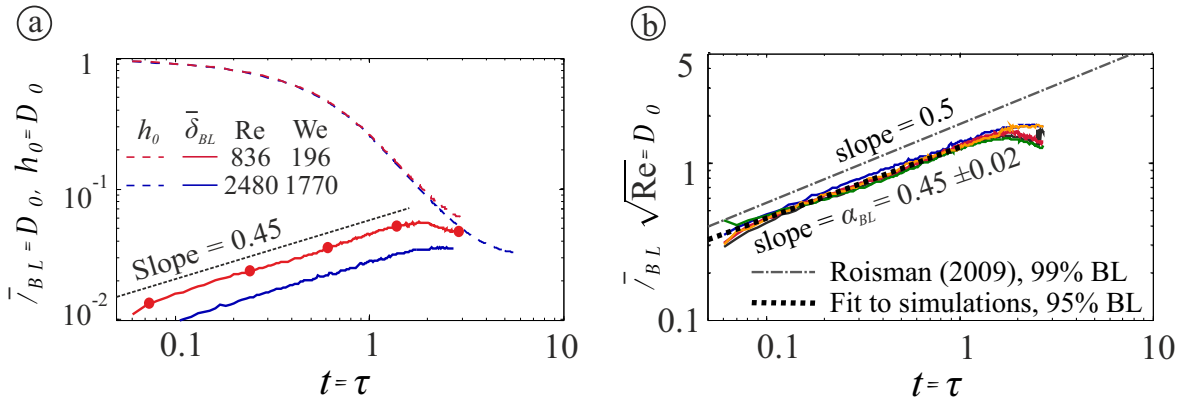
FIG. 12: (a) Simulated space-averaged boundary layer thickness versus time for two (Re, We) pairs (in red and blue, as shown in the legend), normalized by the droplet diameter. The dashed lines indicate the center height of the droplet $h_0(t)$. The red markers correspond to the droplet profiles as plotted in figure 11. Figure (b) shows the boundary layer thicknesses normalized by $Re^{-1/2}$ (line colors indicate Reynolds and Weber numbers as in figure 13 (b)), displaying a good collapse in this normalization.

D. Boundary layer development

During impact, the radial flow over the surface results in the development of a boundary layer from the surface. Here the local boundary layer thickness $\delta_{BL}(r, t)$ is defined as the height at which 95% of the maximal horizontal velocity is reached. The red lines in figure 11 show the boundary layer thickness derived from the simulations, which is generally well-defined (values close to the origin ($r < 5$ μm) and early times ($t/\tau < 0.06$) are inconsistent and therefore excluded). To obtain a single boundary layer thickness value for each instant in time, $\delta(r, t)$ is spatially averaged as:

$$\overline{\delta}_{BL}(t) = \frac{4 \int_0^{2\pi} \int_0^{D(t)/2} \delta_{BL}(r,t)r dr d\theta}{\pi D(t)^2},$$ (3)

with θ the angular coordinate. This spatially-averaged boundary layer thickness is plotted as a function of time in figure 12a. The markers on the red line correspond to the snapshots in figure 11. A maximum boundary layer thickness is observed at $t/\tau \approx 2.5$ when the (increasing) boundary layer thickness approaches the (decreasing) droplet thickness $h_0(t)$ (indicated by the dashed line in figure 12a). This instant is important in the determination of the maximum spreading diameter, as will be discussed in detail in section III F.

The temporal development of the boundary layer was theoretically addressed in the con-

text of droplet impact [37]. There, an analytical flow field solution for inertia-dominated inviscid flow onto a wall (long after initiation) was extended to include viscosity and a no-slip condition on the wall. This results in the development of a boundary layer with an homogeneous thickness over the full surface area (which is surprisingly consistent with figure 11, showing a roughly spatially homogeneous boundary layer thickness for various instants). Based on this model, a 99% boundary layer thickness as a function of time is proposed as:

$$\delta_{99} \approx 1.88 D_0 \sqrt{\frac{t}{\tau \text{Re}}}. \tag{4}$$

which is indicated by the dash-dotted line in figure 12b.

The non-dimensional boundary layer thickness obtained from our simulation is plotted in figure 12b. For a range of Reynolds- and Weber numbers (indicated in the caption), the results collapse to a single curve which confirms the robustness of the boundary layer scaling with respect to the Reynolds number. The curve follows $\overline{\delta}_{BL}(t) \sim D_0 \text{Re}^{-1/2}(t/\tau)^{\alpha_{BL}}$ with exponent $\alpha_{BL} = 0.45 \pm 0.02$, and lies below the prediction of ref. [37]. This latter difference is due to the different definitions of the boundary layers: we assume a 95% boundary layer whereas a 99% boundary layer is used in ref. [37]. Also the exponent $\alpha_{BL} = 0.45 \pm 0.02$ lies slightly below the theoretical exponent of 1/2. This is due to the finite spreading diameter of the droplet: An instantaneous boundary layer development over the full surface is assumed in the theory [37], but the actual boundary layer development is limited to the (growing) area below the droplet. The deviations from the theoretical relationship ($\delta \sim D_0 \sqrt{t/\tau \text{Re}}$) are smaller than the differences originating from different boundary layer thickness definitions. Therefore, for practical purposes, either relationship will adequately describe the boundary layer development in droplet impact.

E.   Rim development

The formation of a pronounced rim is observed both in experiments (figure 6) and simulations (figure 11). To quantify the rim diameter, a circle is fitted to the outermost points of the simulated droplet profile as plotted in figure 11 (dashed white circles collapsing to the rim). The resulting rim diameter is plotted as a function of time in figure 13a, in which the markers show validation measurements from the side-view images which confirm the
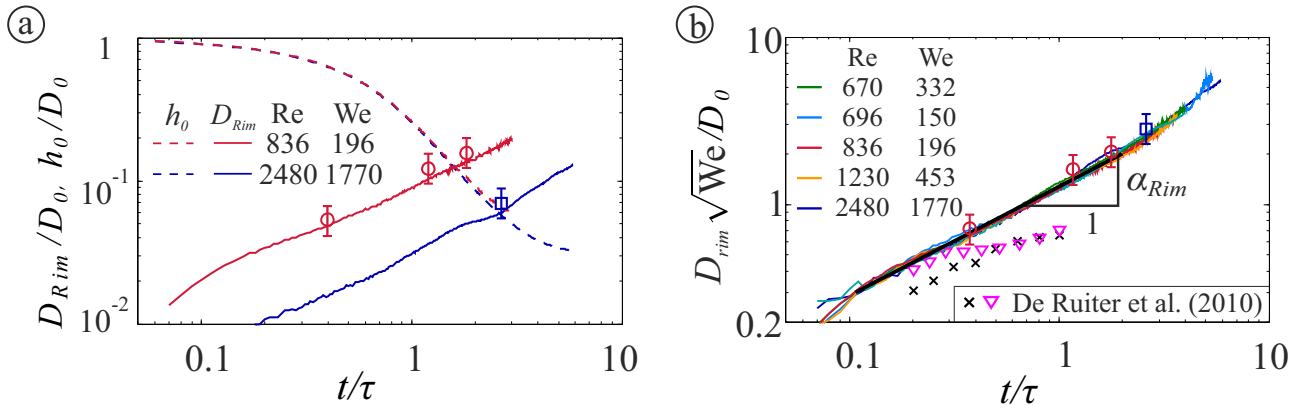
FIG. 13: Simulated rim diameter versus time, for various (Re, We) pairs as shown in the legend. (a) Rim diameter normalized by the droplet diameter as a function of time normalized by the inertial time scale τ. The markers correspond to measured rim diameters. The dashed lines indicate the center height of the droplet $h_0(t)$. Figure (b) shows the rim diameter normalized by $D_0 We^{-1/2}$. Fitting the rim evolution in time provides the exponent $\alpha_{Rim} = 0.68 \pm 0.04$, which is indicated as a black line. Rim height measurements for mm-sized droplets are added in figure (b), from ref. [64], for We = 59 and Re = 1340 (black crosses, $\times$), and We = 185 and Re = 2360 (magenta triangles $\triangledown$).

numerical results.

In figure 13b, the rim radius is normalized by a length scale $D_0 / We^{1/2}$ [64]. This length scale is derived from the position which the rim has reached after a time $\tau = D_0/V_0$, assuming a typical deceleration of V_0^2/D_0 [21, 64]. Using this normalization, all our data collapse to a single curve described by $D_{Rim}/D_0 \sim We^{-1/2}(t/\tau)^{\alpha_{Rim}}$. Fitting our data to this equation provides $\alpha_{Rim} = 0.68 \pm 0.04$. To our knowledge, this remarkably robust scaling exponent (which seems to hold also for times $t/\tau > 1$), has not yet been theoretically explained.

To compare our results to rim size measurements of mm-sized droplets, measurements by De Ruiter et al. [64] are added to figure 13b (as discussed in ref. [64], earlier experimental work on the rim thickness [27, 57, 65–67] is hardly applicable to drop impact on a smooth solid surface). These measurements neither collapse on our data nor our numerical results, but they are of the same order of magnitude. The temporal evolution of the rim diameter could not be uniquely established in ref. [64] as the data set was limited to $0.2 < t/\tau < 1$. However, since droplet impact is generally scale-invariant, and our results partially agree to theory and experiments for mm-sized droplets [64], the herein observed scaling might also describe the rim dynamics of mm-sized droplets.
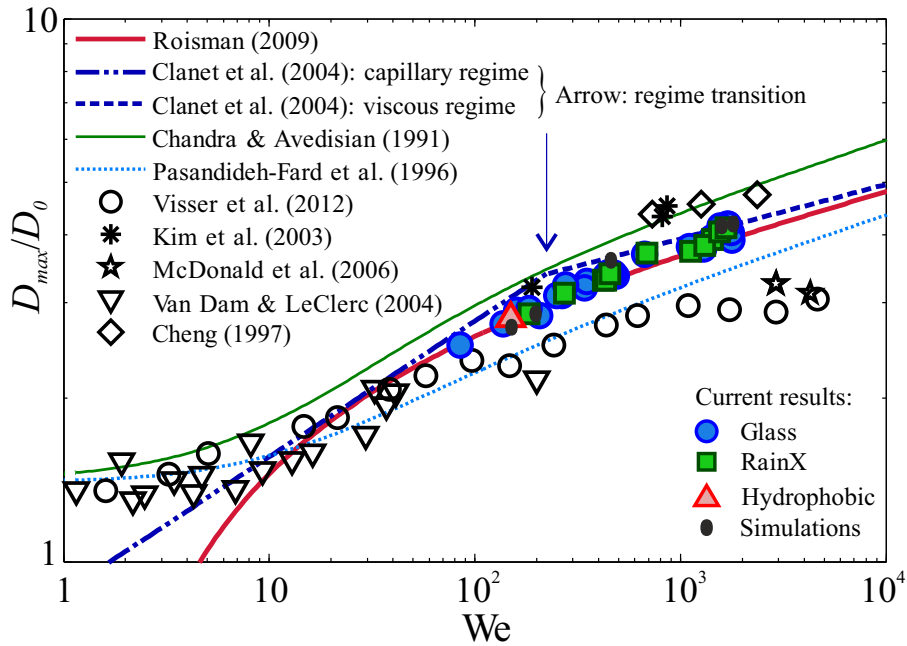
Soft Matter Accepted Manuscript

FIG. 14: Normalized maximum spreading diameter versus the Weber number, for the current experiments (colored markers) and simulations (black dots), other micro-droplet experiments (black markers), and models (lines). The arrow indicates the transition between the capillary- and viscous-regimes proposed in ref. [21].

F.   Maximum spreading diameter

The measured maximum spreading diameter D_{max}/D_0 is plotted in figure 14 and compared to several theoretical [21, 26, 37, 44] and experimental results for microdroplets [3, 14, 15, 20, 31]. For We ≈ 100, good agreement is observed with previous experiments [14, 31]. For larger Weber numbers, the current maximum diameter clearly lies below [15, 20] or above [3, 14, 31] previous work; the differences are discussed in the appendix.

The maximum spreading diameter is the result of a competition of forces. On the one hand, inertia drives the liquid to radially expand. On the other hand, surface tension pulls back the expanding sheet, and viscosity dissipates part of the energy, limiting the maximum spreading diameter. The limiting cases, in which inertia is balanced by either surface tension or viscous dissipation (hereafter called the capillary- and viscous regime, respectively), were separately modeled by Clanet *et al.* [21]. The transition between these regimes is set by the parameter $P = \text{We}/\text{Re}^{4/5} = 1$, as indicated by the arrow in figure 14 and the solid line in figure 2. The model shows good agreement with the current results.

However, two important additional phenomena are affecting the maximum spreading

diameter [26, 36, 37, 54, 68]: (i) the formation of a rim at the edge of the expanding droplet, and (ii) viscous dissipation takes place within a thin boundary layer, as discussed. An improved approach to model spreading at We $\gg 1$ would therefore include inertial spreading limited by boundary layer dissipation and the retraction of a rim. This approach was taken by Roisman [37], where the scaling of $D_{max}/D_0 \sim \mathrm{Re}^{1/5}$ for viscosity-limited spreading is recovered analogous to Ref. [21] (for Re $\gtrsim 100$ and infinite Weber number). This result was generalized for finite Weber numbers (We $\gtrsim 10$) by introducing a correction to account for the growth of the rim, resulting in the following semi-empirical expression for the maximal spreading diameter [37]:

$$D_{max}/D_0 = 0.87\mathrm{Re}^{1/5} - 0.40\mathrm{Re}^{2/5}\mathrm{We}^{-1/2} \tag{5}$$

Excellent agreement with our data is observed (figure 14). As this model was also validated for mm-sized droplets, we conclude that, for a large parameter regime, the maximum spreading diameter is captured by the Weber- and Reynolds numbers alone[2].

G. Splashing

Splashing is not observed in the current and previous [31] measurements for high-speed impact of microdroplets. Empirical splash threshold models sometimes (correctly) predict absence of a splash [69–71], but also the incidence of a splash is frequently predicted for our maximum-velocity impacts [72–74], for which $V_0 = 50$ m/s, $D_0 = 50\mu$m, Re ≈ 2500, and We ≈ 1770, surface roughness $R_a = 5$nm, and water and air at atmospheric pressure are used.

These conflicting results clearly indicate a need for improving the physical understanding of splashing, on which great progress has recently been made. The consensus is that splashing is caused by ejection and upward deflection of the liquid lamella forming during impact [56, 75]. In particular, two splash mechanisms have been proposed. First, the lamella may

---

[2] As discussed in ref. [26], excluding the boundary layer generally results in an over-prediction of D_{max}. In this view, the excellent agreement between our measurements and the basic model from ref. [21] is surprising. However, as the spreading stops when the boundary layer equals the lamella thickness, assuming the lamella thickness as the relevant viscous length scale (instead of explicitly incorporating the boundary layer) results in a very minor error.

be deflected upwards by liquid touchdown on the substrate. This touchdown results in a local boundary layer, which has a "bump"-shape deflecting the ejected lamella away from the surface [75]. The impact velocity threshold beyond which splashing occurs is proposed to equal the critical impact velocity for lamella ejection, provided as [75]:

$$V_{th} = C \left(\frac{2\sigma^3}{\mu_g^2 \rho D_0} \right)^{1/4} \quad , \quad 0.1 < C < 0.3 \tag{6}$$

providing $8.9 < V_{th} < 27$ m/s for our system, i.e. the predicted threshold velocity is too low. However, surface roughness and air compressibility may influence the actual threshold [75]. Extrapolating figure 8 from [75] indicates that roughness on a 1 nm-scale (which is of the order of our glass substrate roughness) is expected to further decrease the splash threshold impact velocity. Another factor which potentially suppresses splashing for the current small-scale droplets is that the touchdown occurs in a different way as compared to the model in [75], since the air film thickness is expected to become thinner than ~ 10 times the mean free path length of the gas molecules. In this regime the droplet's touchdown is highly nontrivial. Although the subtleties for this case have been discussed in detail for mm-sized droplets [75], they may be different for the current regime. Extending this model to fast microdroplet impact would provide an opportunity for further validation.

A second proposed splash threshold is based on a competition between destabilization of the lamella by the air film under the droplet, and the stabilizing effect of surface tension [32]. This model (which is based on dimensional analysis, and therefore does not explicitly include any physical mechanisms) predicts splashing for

$$V_0 \gtrsim \frac{\rho \sigma^2 k_B T}{\gamma \mu M_G P^2 D_0} \tag{7}$$

with k_B Boltzmann's constant, T the temperature, M_G the molecular weight of the gas, γ the adiabatic constant of the gas, and P the pressure of the ambient air. For our 50 μm-droplets in air, this yields a splashing threshold velocity of ~ 500 m/s, thus no splashing is predicted for our droplets with impact velocities up to 50 m/s.

Recently, a similar approach has been translated into a complete physical model. Here, the lift-off of the lamella is assumed to be governed by the air surrounding the droplet (by both air compression below the lamella and a lift force due to a low-pressure area above

the lamella) [56]. Another key ingredient is the (growing) rim diameter. If the lamella is lifted faster than the rim grows, the rim will not touch the substrate and splashing is predicted. However, if the rim diameter increases faster than the lamella lifts away from the surface, the rim will touch the substrate and splashing is suppressed. This model successfully predicts the splash threshold of mm-sized droplets, for a variety of liquids. However, a key model assumption is that the air film thickness exceeds the mean free path length of the gas molecules. As this condition is violated here, a prediction cannot be obtained for our control parameters.

As yet, our observation of non-splashing impact is predicted only by empirical models [32, 69, 70]. As the model by Xu *et al.* [32] contains most physical insights and has been successfully extended to explain the splash threshold of droplets impacting on hot surfaces [29], it seems to be the best splash prediction model as yet. However, since only scaling arguments are used, details of the physics of splashing remain to be understood. Recent attempts provide validated splash threshold predictions for mm-sized droplets [56, 75], but neither of these approaches is applicable to the micrometer domain since the continuum assumption of the gas breaks down. As the underlying physics of these models are fundamentally different, details of the splash mechanism remain to be fully understood and future modeling efforts are expected. The current results, in which no splash is observed despite high impact velocities, may provide a powerful tool for validating these models.

IV. CONCLUSIONS

In this work the similarities and differences between mm-sized droplet impact (for which great progress has been made recently) and micrometer-sized droplet impact (which is key for industrial applications but has hardly been addressed) are studied in detail. Highly reproducible micrometer-scale droplets were generated and visualized using flash-illumination. Side-view images show the spreading droplet at a temporal resolution exceeding 10^7 frames per second. Bottom-view images reveal a fringe pattern due to reflection of the (flat) glass interface and the (curved) top surface of the droplet, and were used to resolve the droplet shape at sub-micron resolution. A numerical model is developed and extensively validated using the side-and bottom-view measurements. The model is used to study the boundary layer development and the size of the rim, which are challenging to quantify experimentally.

The spreading dynamics, droplet-air interaction, boundary layer development, rim development, maximum droplet spreading diameter, and splashing threshold are investigated in detail. The main conclusions are:

1. The spreading dynamics can be divided into different phases. The initial phase, prior to the ejection of a lamella, could not be investigated due to the extremely short time scales involved. In the lamella phase, a scaling $D/D_0 \sim \sqrt{t/\tau}$ is observed, which is in quantitative agreement with ref. [57]. The final (slow-down) phase results in the maximal spreading diameter, see item 5.

2. The air bubble size entrained during microdroplet impact decreases with increasing impact velocities (for the currently studied impact velocities $V_0 > 10$ m/s). The scaling of the air bubble size collapses to results for mm-sized droplet impact in the high-Stokes number regime. The threshold Stokes number separating the high- and low Stokes number regimes is different, which is expected since this parameter is size-dependent.

3. The boundary layer thickness scales as $\overline{\delta}_{BL}(t) \sim D_0 \mathrm{Re}^{-1/2}(t/\tau)^\alpha$ with an effective exponent $\alpha_{BL} = 0.45 \pm 0.02$. The Reynolds number dependence follows the expected scaling of $\overline{\delta}_{BL}(t) \sim D_0 \mathrm{Re}^{-1/2}\sqrt{t/\tau}$, but the temporal progression is somewhat lower. In addition, details of the definition of the boundary layer have a pronounced effect, which is expected to influence variables which depend on the boundary-layer thickness.

4. The rim diameter follows a scaling $D_{Rim}/D_0 \sim \mathrm{We}^{-1/2}(t/\tau)^{\alpha_{Rim}}$, with effective exponent $\alpha_{Rim} = 0.68 \pm 0.04$. To our knowledge, this scaling is observed for the first time. The temporal exponent and the remarkable robustness of this scaling for times $t/\tau > 1$ remain to be explained.

5. The maximal droplet spreading diameter is robustly captured by models balancing the inertia of the droplet to viscous dissipation in the boundary layer [37].

6. Despite our high impact velocities up to $V_0 = 50$ m/s, no splash is observed here. Only the model by Xu et al. [32] correctly predicts this outcome. This model is based on scaling arguments, and does not contain detailed (force) balances and prefactors. Alternative models capture the physics of splashing in more detail [56, 75], but since

the continuum assumption is violated for the thin air film between the droplet and the substrate these models cannot be applied here.

As far as could be observed, droplet impact is scale-invariant, i.e. mm-sized droplet experiments have a predictive value as long as the same Reynolds, Weber, and Stokes number are used. Therefore, the vast progress in understanding mm-sized droplet impact can be applied to optimize a wide range of applications in which fast, μm-sized droplet impact on a dry surface is a key process step, such as (3D)(bio)printing, thermal spraying, spray cleaning, and laser-induced forward transfer. Future studies may address additional phenomena including lamella break-up [76], the influence of the slip length [54, 76], and droplet compressibility [76, 77] as these are highly relevant for impact of even faster and smaller droplets [76].

APPENDIX A: EXPLANATION OF DIFFERENCES AMONG EXPERIMENTAL RESULTS OF DROPLET SPREADING

Figure 14 shows the normalized maximum spreading diameter. For We > 100, the current maximum diameter clearly lies below [15, 20] or above [3, 14, 31] previous work; the discrepancies are discussed here.

The results exceeding our results were taken for droplets with $D_0 = 235 \pm 30$μm [15] and $D_0 = 230$μm [20], i.e. larger than our droplets with $D_0 = 48 \pm 3$μm. As the spreading depends on both We and Re (and not on We alone as displayed in the graph), a larger spreading is expected. Assuming We = 800 and droplet diameters $D_0 = [48, 235]$μm, we obtain Re = [1661, 3666], respectively. Using the model of Roisman [37], a 15% larger spreading diameter is expected for the larger ($D_0 = 230$μm) droplets. The data around We = 800 shows a 20% increase, i.e. a slightly larger but similar value.

Our previous results [31] are clearly lower than the current results (at We = 800, a 21%
decrease is found). This is due to three reasons. First, the high-Weber number measurements
were taken for smaller droplets ($\sim$ 20μm), as the previous droplet generation method did
not produce consistent droplet sizes for all velocities (ref. [31], figure 2c). An analysis
similar to the previous paragraphs shows an expected decrease in spreading diameter of
5%. Second, the current measurements show that the maximum spreading is reached by
the cylindrical rim, i.e. above the surface. Just after reaching its maximum spreading the
rim retracts around 3%, while (for hydrophilic surfaces) the contact line initially sticks to
the surface. The temporal resolution of the previous measurements (1μs) did not allow
to visualize this retraction, and thus in the previous measurement the maximum wetted
diameter was measured instead of the maximum extension of the rim. This also accounts
for a part of the discrepancy. Finally, the spatial resolution of the previous experiments was
much more limited (ref. [31], figure 3d). In that work we appear to have over-estimated
the measurement accuracy at the droplet edge, and we now conclude that high-resolution
measurements are required for adequate spreading measurements. As this problem worsens
with increasing velocities, the plateau of D_{max}/D_0 reported for We > 1000 [20, 31] requires
validation.

Then, the maximum spreading of hot metal droplets onto a glass surface (ref. [3], figure
3b) also lies below current results. As the glass temperature was much below the metal
melting temperature, solidification might have limited the spreading diameter. In addition,
the surface tension of a hot ($\sim$ 3300K) droplet while cooling down and oxidizing is hard to
establish, i.e. the Weber number is poorly defined. Here we take a value of $\sigma = 2.3\mathrm{N/m}$ from
ref. [78] and estimate $\sigma = 2.0\mathrm{N/m}$ for the steel-chromium alloy reported [79], as values for
the actual alloy may not exist. Finally, the initial droplet diameter had a high uncertainty
(Particles with $D_0 = 60 \pm 38$μm with an average of $D_0 = 40$μm were reported). Although
a 40-measurement average was taken, this could strongly add to the error. Therefore, in
view of these major uncertainties, we are surprised by the reasonable agreement with our
measurements.

Finally, one data point from previous high-quality measurements [14] lies significantly
below our data. As this single data point also lies below the curve plotted in ref. [14],
we took a detailed look at the experimental parameters. The authors report a maximum
impact velocity of $V_0 = 13.8$ m/s and a maximum diameter of $D_0 = 42$μm, corresponding

to We = 111 for water. However, the data point was plotted at We $\approx$ 200, resulting in a minor discrepancy. In conclusion, we think the current results are at least as reliable as (and mostly consistent with) previous work.

———————————————

[1] S. W. Park and C. S. Lee, *Macroscopic and microscopic characteristics of a fuel spray impinged on the wall*, Experiments in Fluids **37**, 745 (2004).

[2] A. Moreira, A. Moita, and M. Panão, *Advances and challenges in explaining fuel spray impingement: How much of single droplet impact research is useful?*, Progress in Energy and Combustion Science **36**, 554 (2010).

[3] A. McDonald, M. Lamontagne, C. Moreau, and S. Chandra, *Impact of plasma-sprayed metal particles on hot and cold glass surfaces*, Thin Solid Films **514**, 212 (2006).

[4] H. Troesch, *Die Zerstäubung von Flüssigkeiten*, Chemie Ingenieur Technik (1954).

[5] D. Attinger, Z. Zhao, and D. Poulikakos, *An experimental study of molten microdroplet surface deposition and solidification: Transient behavior and wetting angle dynamics*, Journal of Heat Transfer **122**, 544 (2000).

[6] S. Tasoglu and U. Demirci, *Bioprinting for stem cell research.*, Trends in Biotechnology **31**, 10 (2013).

[7] T. Boland, X. Tao, B. J. Damon, B. Manley, P. Kesari, S. Jalota, and S. Bhaduri, *Drop-on-demand printing of cells and materials for designer tissue constructs*, Materials Science and Engineering: C **27**, 372 (2007).

[8] B. Guillotin, A. Souquet, S. Catros, M. Duocastella, B. Pippenger, S. Bellance, R. Bareille, M. Rémy, L. Bordenave, J. Amédée, and F. Guillemot, *Laser assisted bioprinting of engineered tissue with high cell density and microscale organization.*, Biomaterials **31**, 7250 (2010).

[9] A. Klini, P. A. Loukakos, D. Gray, A. Manousaki, and C. Fotakis, *Laser induced forward transfer of metals by temporally shaped femtosecond laser pulses.*, Optics Express **16**, 11300 (2008).

[10] J. Schlabe, C. Johnen, R. Schwartlander, V. Moser, B. Hartmann, J. C. Gerlach, and M. V. Küntscher, *Isolation and culture of different epidermal and dermal cell types from human scalp suitable for the development of a therapeutical cell spray.*, Burns : Journal of the International Society for Burn Injuries **34**, 376 (2008).

[11] H. F. Okorn-Schmidt, F. Holsteyns, a. Lippert, D. Mui, M. Kawaguchi, C. Lechner, P. E. Frommhold, T. Nowak, F. Reuter, M. B. Pique, C. Cairos, and R. Mettin, *Particle cleaning technologies to meet advanced semiconductor device process requirements*, ECS Journal of Solid State Science and Technology **3**, N3069 (2013).

[12] W. Melfo, H. Bolt, M. Rijnders, D. Staalman, C. B. Castro, D. Crowther, and B. Jana, *Experimental study on primary scale formation and descalability on steels containing Ni and Ni+Si*, ISIJ International **53**, 866 (2013).

[13] M. Versluis, *High-speed imaging in fluids*, Experiments in Fluids **54**, 1458 (2013).

[14] D. B. van Dam and C. Le Clerc, *Experimental study of the impact of an ink-jet printed droplet on a solid substrate*, Physics of Fluids **16**, 3403 (2004).

[15] H.-Y. Kim, S.-Y. Park, and K. Min, *Imaging the high-speed impact of microdrop on solid surface*, Review of Scientific Instruments **74**, 4930 (2003).

[16] S. Jung and I. M. Hutchings, *The impact and spreading of a small liquid drop on a non-porous substrate over an extended time scale*, Soft Matter **8**, 2686 (2012).

[17] R. C. A. van der Veen, T. Tran, D. Lohse, and C. Sun, *Direct measurements of air layer profiles under impacting droplets using high-speed color interferometry*, Physical Review E **85**, 026315 (2012).

[18] R. Bhola and S. Chandra, *Parameters controlling solidification of molten wax droplets falling on a solid surface*, Journal of Materials Science **4**, 4883 (1999).

[19] W. Bouwhuis, R. C. A. van der Veen, T. Tran, D. L. Keij, K. G. Winkels, I. R. Peters, D. van der Meer, C. Sun, J. H. Snoeijer, and D. Lohse, *Maximal air bubble entrainment at liquid-drop impact*, Physical Review Letters **109**, 264501 (2012).

[20] L. Cheng, *Dynamic spreading of drops impacting onto a solid surface*, Industrial & Engineering Chemistry Process Design Development **16**, 192 (1977).

[21] C. Clanet, C. Béguin, D. Richard, and D. Quéré, *Maximal deformation of an impacting drop*, Journal of Fluid Mechanics **517**, 199 (2004).

[22] R. Ford and C. Furmidge, *Impact and spreading of spray drops on foliar surfaces*, Soc Chem Ind Monogr 417 (1967).

[23] H. Fukanuma and A. Ohmori, in *Proc. Natl. Therm. Spray Conf.* (ASM International, Boston, MA, 1994), pp. 563–568.

[24] G. Lagubeau, M. A. Fontelos, C. Josserand, A. Maurel, V. Pagneux, and P. Petitjeans, *Spread-*

ing dynamics of drop impacts, Journal of Fluid Mechanics **713**, 50 (2012).

[25] H. Marmanis and S. T. Thoroddsen, *Scaling of the fingering pattern of an impacting drop*, Physics of Fluids **8**, 1344 (1996).

[26] M. Pasandideh-Fard, Y. M. Qiao, S. Chandra, and J. Mostaghimi, *Capillary effects during droplet impact on a solid surface*, Physics of Fluids **8**, 650 (1996).

[27] C. D. Stow and M. G. Hadfield, *An experimental investigation of fluid flow resulting from the impact of a water drop with an unyielding dry surface*, Proceedings of the Royal Society A **373**, 419 (1981).

[28] S. Thoroddsen and J. Sakakibara, *Evolution of the fingering pattern of an impacting drop*, Physics of Fluids **10**, 1359 (1998).

[29] T. Tran, H. J. J. Staat, A. Prosperetti, C. Sun, and D. Lohse, *Drop impact on superheated surfaces*, Physical Review Letters **108**, 036101 (2012).

[30] P. Tsai, R. C. A. van der Veen, M. van de Raa, and D. Lohse, *How micropatterns and air pressure affect splashing on surfaces.*, Langmuir **26**, 16090 (2010).

[31] C. W. Visser, Y. Tagawa, C. Sun, and D. Lohse, *Microdroplet impact at very high velocity*, Soft Matter **8**, 10732 (2012).

[32] L. Xu, W. Zhang, and S. Nagel, *Drop splashing on a dry smooth surface*, Physical Review Letters **94**, 184505 (2005).

[33] L. Xu, L. Barcos, and S. Nagel, *Splashing of liquids: Interplay of surface roughness with surrounding gas*, Physical Review E **76**, 066311 (2007).

[34] M. Rein, *Phenomena of liquid drop impact on solid and liquid surfaces*, Fluid Dynamics Research **12**, 61 (1993).

[35] A. Yarin, *Drop impact dynamics: Splashing, spreading, receding, bouncing*, Annu. Rev. Fluid Mech. **38**, 159 (2006).

[36] J. Eggers, M. a. Fontelos, C. Josserand, and S. Zaleski, *Drop dynamics after impact on a solid wall: Theory and simulations*, Physics of Fluids **22**, 062101 (2010).

[37] I. V. Roisman, *Inertia dominated drop collisions. II. An analytical solution of the Navier-Stokes equations for a spreading viscous film*, Physics of Fluids **21**, 052104 (2009).

[38] J. M. Kolinski, S. M. Rubinstein, S. Mandre, M. P. Brenner, D. A. Weitz, and L. Mahadevan, *Skating on a film of air: Drops impacting on a surface*, Physical Review Letters **108**, 074503 (2012).

[39] M. M. Driscoll and S. R. Nagel, *Ultrafast interference imaging of air in splashing dynamics*, Physical Review Letters **107**, 154502 (2011).

[40] S. Mandre, M. Mani, and M. P. Brenner, *Precursors to splashing of liquid droplets on a solid surface.*, Physical Review Letters **102**, 134502 (2009).

[41] M. Mani, S. Mandre, and M. Brenner, *Events before droplet splashing on a solid surface*, Journal of Fluid Mechanics **647**, 163 (2010).

[42] S. T. Thoroddsen, T. G. Etoh, K. Takehara, N. Ootsuka, and Y. Hatsuki, *The air bubble entrapped under a drop impacting on a solid surface*, Journal of Fluid Mechanics **545**, 203 (2005).

[43] J. S. Lee, B. M. Weon, J. H. Je, and K. Fezzaa, *How does an air film evolve into a bubble during drop impact?*, Physical Review Letters **109**, 204501 (2012).

[44] S. Chandra and C. T. Avedisian, *On the dollision of a droplet with a solid surface*, Proceedings of the Royal Society A: Mathematical, Physical and Engineering Sciences **432**, 13 (1991).

[45] V. Mehdi-Nejad, J. Mostaghimi, and S. Chandra, *Air bubble entrapment under an impacting droplet*, Physics of Fluids **15**, 173 (2003).

[46] S. D. Aziz and S. Chandra, *Impact, recoil and splashing of molten metal droplets*, International Journal of Heat and Mass Transfer **43**, 2841 (2000).

[47] D. Richard, C. Clanet, and D. Quéré, *Contact time of a bouncing drop*, Nature **417**, 811 (2002).

[48] M. Reyssat, D. Richard, C. Clanet, and D. Quéré, *Dynamical superhydrophobicity*, Faraday Discussions **146**, 19 (2010).

[49] A. Checco, P. Guenoun, and J. Daillant, *Nonlinear Dependence of the Contact Angle of Nanodroplets on Contact Line Curvature*, Physical Review Letters **91**, 186101 (2003).

[50] N. R. Lindblad and J. M. Schneider, *Production of uniform-sized liquid droplets*, Journal of Scientific Instruments **42**, 635 (1965).

[51] P. E. Frommhold, A. Lippert, F. L. Holsteyns, and R. Mettin, *High-speed monodisperse droplet generation by ultrasonically controlled micro-jet breakup*, Experiments in Fluids **55**, 1716 (2014).

[52] P. Kim, M. J. Kreder, J. Alvarenga, and J. Aizenberg, *Hierarchical or not? Effect of the length scale and hierarchy of the surface roughness on omniphobicity of lubricant-infused substrates*, Nano Letters **13**, 1793 (2013).

33

[53] S. Popinet, *An accurate adaptive solver for surface-tension-driven interfacial flows*, Journal of Computational Physics **228**, 5838 (2009).

[54] H. Lastakowski, F. Boyer, a. L. Biance, C. Pirat, and C. Ybert, *Bridging local to global dynamics of drop impact onto solid substrates*, Journal of Fluid Mechanics **747**, 103 (2014).

[55] R. Rioboo, M. Marengo, and C. Tropea, *Time evolution of liquid drop impact onto solid, dry surfaces*, Experiments in Fluids **33**, 112 (2002).

[56] G. Riboux and J. M. Gordillo, *Experiments of drops impacting a smooth solid surface: A model of the critical impact speed for drop splashing*, Physical Review Letters **113**, 024507 (2014).

[57] A. Mongruel, V. Daru, F. Feuillebois, and S. Tabakova, *Early post-impact time dynamics of viscous drops onto a solid dry surface*, Physics of Fluids **21**, 032101 (2009).

[58] H.-Y. Kim, Z. C. Feng, and J.-H. Chun, *Instability of a liquid jet emerging from a droplet upon collision with a solid surface*, Physics of Fluids **12**, 531 (2000).

[59] H. Wagner, *Phenomena associated with impacts and sliding on liquid surfaces*, Z. Angew. Math. Mech **4**, (1932).

[60] P. D. Hicks and R. Purvis, *Air cushioning in droplet impacts with liquid layers and other droplets*, Physics of Fluids **23**, 062104 (2011).

[61] J. M. Kolinski, L. Mahadevan, and S. M. Rubinstein, *Lift-off instability during the impact of a drop on a solid surface*, Physical Review Letters **112**, 134501 (2014).

[62] A. Eddi, K. G. Winkels, and J. H. Snoeijer, *Short time dynamics of viscous drop spreading*, Physics of Fluids **25**, 013102 (2013).

[63] P. D. Hicks and R. Purvis, *Liquid-solid impacts with compressible gas cushioning*, Journal of Fluid Mechanics **735**, 120 (2013).

[64] J. de Ruiter, R. E. Pepper, and H. A. Stone, *Thickness of the rim of an expanding lamella near the splash threshold*, Physics of Fluids **22**, 022104 (2010).

[65] D. C. D. Roux and J. J. Cooper-White, *Dynamics of water spreading on a glass surface*, Journal of Colloid and Interface Science **277**, 424 (2004).

[66] I. V. Roisman, K. Horvat, and C. Tropea, *Spray impact: Rim transverse instability initiating fingering and splash, and description of a secondary spray*, Physics of Fluids **18**, 102104 (2006).

[67] E. Villermaux and B. Bossa, *Drop fragmentation on impact*, Journal of Fluid Mechanics **668**, 412 (2011).

[68] S. Tabakova, F. Feuillebois, A. Mongruel, V. Daru, and S. Radev, *First stages of drop impact on a dry surface: Asymptotic model*, Zeitschrift für angewandte Mathematik und Physik **63**, 313 (2012).

[69] R. L. V. Wal, G. M. Berger, and S. D. Mozes, *The splash/non-splash boundary upon a dry surface and thin fluid film*, Experiments in Fluids **40**, 53 (2005).

[70] C. S. Stevens, *Scaling of the splash threshold for low-viscosity fluids*, EPL (Europhysics Letters) **106**, 24001 (2014).

[71] K.-L. Pan, K.-C. Tseng, and C.-H. Wang, *Breakup of a droplet at high velocity impacting a solid surface*, Experiments in Fluids **48**, 143 (2009).

[72] C. Mundo, M. Sommerfeld, and C. Tropea, *Droplet-wall collisions: Experimental studies of the deformation and breakup process*, International Journal of Multiphase Flow **21**, 151 (1995).

[73] K. Range and F. Feuillebois, *Influence of surface roughness on liquid drop impact*, Journal of Colloid and Interface Science **30**, 16 (1998).

[74] G. E. Cossali, a. Coghe, and M. Marengo, *The impact of a single drop on a wetted solid surface*, Experiments in Fluids **22**, 463 (1997).

[75] S. Mandre and M. Brenner, *The mechanism of a splash on a dry solid surface*, Journal of Fluid Mechanics **690**, 148 (2012).

[76] R. Zhang, S. Farokhirad, T. Lee, and J. Koplik, *Multiscale liquid drop impact on wettable and textured surfaces*, Physics of Fluids **26**, 082003 (2014).

[77] J. Field, J. Dear, and J. Ogren, *The effects of target compliance on liquid drop impact*, Journal of Applied Physics **65**, 533 (1989).

[78] W. M. Haynes, D. R. Lide, and T. J. Bruno, *CRC Handbook of Chemistry and Physics* (CRC Press, Boca Raton, Fl, USA, 2012).

[79] K. Mukai, L. Zushu, and M. Zeze, *Surface tension and wettability of liquid Fe-16 mass % Cr-O alloy with alumina*, Materials Transactions **43**, 1724 (2002).
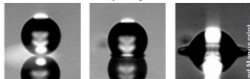
Droplet impact
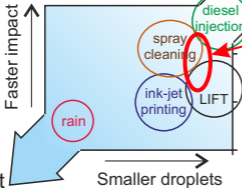
Soft Matter

Our experiments

and simulations